

Measuring Photoexcited Free Charge Carriers in Mono- to Few-Layer Transition-Metal Dichalcogenides with Steady-State Microwave Conductivity

Jeffrey L. Blackburn,^{*,†} Hanyu Zhang,[†] Alexis R. Myers,^{†,‡} Jeremy R. Dunklin,[†] David C. Coffey,[§] Rebecca N. Hirsch,[‡] Derek Vigil-Fowler,[†] Seok Joon Yun,^{||} Byeong Wook Cho,^{||,⊥} Young Hee Lee,^{||,⊥} Elisa M. Miller,[†] Garry Rumbles,^{†,#} and Obadiah G. Reid^{*,†,#}

[†]Chemistry and Nanoscience Center, National Renewable Energy Laboratory, 15013 Denver West Parkway, Golden, Colorado 80401, United States

[‡]Department of Chemistry and Biochemistry, University of Colorado Boulder, Boulder, Colorado 80309, United States

[§]Department of Physics, Warren Wilson College, 701 Warren Wilson Road, Swannanoa, North Carolina 28778, United States

^{||}Center for Integrated Nanostructure Physics (CINAP), Institute for Basic Science (IBS), Suwon 16419, Republic of Korea

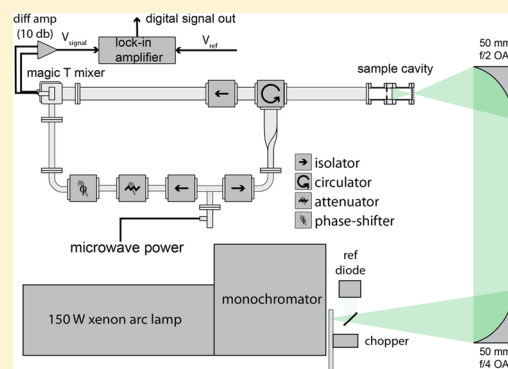
[⊥]Department of Energy Science, Sungkyunkwan University, Suwon 16419, Republic of Korea

[#]Renewable and Sustainable Energy Institute, University of Colorado Boulder, Boulder, Colorado 80309, United States

Supporting Information

ABSTRACT: Photoinduced generation of mobile charge carriers is the fundamental process underlying many applications, such as solar energy harvesting, solar fuel production, and efficient photodetectors. Monolayer transition-metal dichalcogenides (TMDCs) are an attractive model system for studying photoinduced carrier generation mechanisms in low-dimensional materials, because they possess strong direct band gap absorption and large exciton binding energies and are only a few atoms thick. While a number of studies have observed charge generation in neat TMDCs for photoexcitation at, above, or even below the optical band gap, the role of nonlinear processes (resulting from high photon fluences), defect states, excess charges, and layer interactions remains unclear. In this study, we introduce steady-state microwave conductivity (SSMC) spectroscopy for measuring charge generation action spectra in a model WS₂ mono- to few-layer TMDC system at fluences that coincide with the terrestrial solar flux.

Despite utilizing photon fluences well below those used in previous pump-probe measurements, the SSMC technique is sensitive enough to easily resolve the photoconductivity spectrum arising in mono- to few-layer WS₂. By correlating SSMC with other spectroscopy and microscopy experiments, we find that photoconductivity is observed predominantly for excitation wavelengths resonant with the excitonic transition of the multilayer portions of the sample, the density of which can be controlled by the synthesis conditions. These results highlight the potential of layer engineering as a route toward achieving high yields of photoinduced charge carriers in neat TMDCs, with implications for a broad range of optoelectronic applications.



Transition-metal dichalcogenides (TMDCs) are two-dimensional layered materials with highly tunable optoelectronic properties.^{1,2} The band structure of TMDCs varies from metallic to semimetallic to semiconducting² and depends critically upon the dominant transition metal,³ isovalent or aliovalent substitutional dopants,^{4,5} alloying,⁶ and material dimensionality.⁷ Many layered 2D TMDCs, such as MoX₂ and WX₂ (where X = S, Se), transition from indirect band gap semiconductors in their bulk form to direct band gap semiconductors at the monolayer level.^{3,7,8} The large optical absorption cross sections and high charge carrier mobilities of these monolayer TMDCs open up intriguing possibilities for optoelectronic applications, such as solar energy harvesting,^{9–12} photodetectors,^{13,14} and phototransistors.¹⁵ Additionally, the

conduction and valence band energies of several of these TMDCs lie in the appropriate positions for important electrochemical transformations, such as the hydrogen evolution reaction (HER) and oxygen evolution reaction (OER),¹⁶ spurring interest in their potential application in electro- and photocatalytic (e.g., solar-driven) fuel generation schemes.^{17–20} Quantum confinement and reduced dielectric screening in direct band gap monolayer TMDCs give rise to strong electron-hole Coulomb attraction, resulting in the production of strongly bound excitons and/or trions (exciton bound to a charge

Received: October 23, 2019

Accepted: December 2, 2019

Published: December 2, 2019

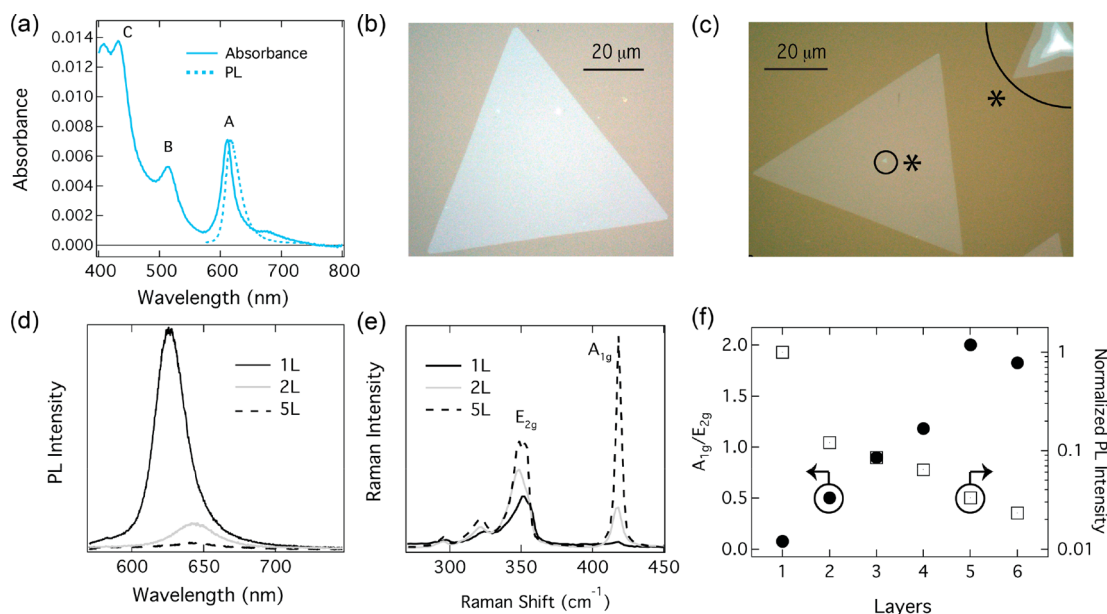


Figure 1. (a) Absorbance (solid line) and confocal photoluminescence (dashed line) spectra of WS₂ sample that is predominantly monolayer (“S-poor 1” sample, vide infra). (b) Optical microscopy image of a monolayer WS₂ flake. (c) Optical microscopy image of WS₂ flakes showing a small triangular second layer in the center of the main large flake and a five-layer flake in the upper right-hand corner. (d) Confocal PL spectra of a WS₂ flake (see Figure S1 for image) containing six layers. PL spectra are taken at locations where different layer numbers (denoted in legend) are visible by optical microscopy. (e) Raman spectra of same WS₂ flake, taken in the same locations as in panel d (see also Figure S1). Excitation is at 532 nm. (f) Dependence of A_{1g}/E_{2g} Raman ratio (left axis) and PL intensity (right axis) on number of WS₂ layers.

59 carrier) for photoexcitation at or above the optical band
60 gap.^{21–24}

61 The crucial first step in using excitonic TMDC semi-
62 conductors for solar energy-harvesting applications is to
63 dissociate excitons into long-lived free charge carriers. One
64 general approach for achieving photoinduced exciton dissoci-
65 ation in excitonic semiconductors is to generate heterojunctions
66 that establish a thermodynamic driving force for interfacial
67 photoinduced charge transfer,^{25–27} and this approach has been
68 applied recently to a number of TMDCs.^{9–11,28–32} Even in the
69 absence of such a heterojunction, there can be non-negligible
70 charge generation in low-dimensional semiconductors with
71 exciton binding energies of several hundred millielectron
72 volts^{14,33–35} because of a pronounced interaction of (often
73 highly mobile) photogenerated excitons with the surrounding
74 environment and/or defect or trap states.³⁶ Some recent studies
75 have observed photoinduced charge generation in neat
76 monolayer TMDCs via pump–probe measurements, such as
77 time-resolved terahertz spectroscopy (TRTS),^{34,35} or via the
78 observation of photoconductivity in, for example, photo-
79 detectors.¹⁴ Charge generation mechanisms are often attributed
80 to the involvement of defect/trap states,^{34,35} and the generated
81 charge carriers tend to recombine rapidly, in the range of 350 fs
82 to 100 ps.^{14,34,35} However, it is important to note that typical
83 time-resolved optical measurements suffer from the use of high
84 photon fluences that can exacerbate nonlinear processes such as
85 multiphoton absorption,^{37,38} band gap renormalization,^{39–41}
86 and multiparticle collisional (Auger) processes.⁴² Typical
87 electrode-based photoconductivity measurements can suffer
88 from the potentially confounding effects of the semiconductor/
89 electrode interface and the influence of applied electric fields.
90 Furthermore, because many pump–probe experiments probe
91 collections of many isolated TMDC flakes that may have varying
92 degrees of monolayer purity (i.e., varying percentages of flakes

with additional layers), the role of these multilayer areas in
59 charge generation remains unclear.
60

To address these issues, we introduce in this study a low-
95 fluence contact-less method for measuring photoconductivity in
96 mono- to few-layer TMDCs, based on the absorption of
97 microwave radiation by charge carriers generated under
98 conditions of steady-state illumination. The technique, steady-
99 state microwave conductivity (SSMC),⁴³ shares many of the
100 advantages of flash-photolysis time-resolved microwave con-
101 ductivity (fp-TRMC), which our group and others have used to
102 study charge generation in a wide variety of neat semiconductors
103 and heterostructured systems.^{27,33,44–47} In general, the use of a
104 resonant cavity in microwave conductivity experiments
105 enhances the sensitivity for measuring photoconductivity
106 relative to TRTS, allowing for the use of substantially lower
107 excitation fluences. Furthermore, the continuous wave (CW)
108 light source utilized for SSMC enables the use of a higher quality
109 factor cavity and lock-in detection to achieve operation at even
110 lower fluence values than employed by the pulsed light source of
111 a typical fp-TRMC experiment. Our SSMC experiment operates
112 at fluences ($\sim 1 \times 10^{14}$ cm²/s/nm @ 600 nm) somewhat below
113 those associated with terrestrial solar flux ($\sim 4 \times 10^{14}$ cm²/s/nm
114 @ 600 nm). Here, we use the SSMC technique to explore the
115 photoconductivity action spectrum of a model WS₂ TMDC
116 system. We find that the dominant photoconductivity response
117 occurs for excitation of the A exciton transition of small
118 multilayer areas of WS₂. The intensity of this transition, and by
119 extension the total charge density created in the WS₂ flakes,
120 can be tuned via the sulfur feeding rate used in the chemical vapor
121 deposition (CVD) synthesis. These results introduce both a
122 powerful new method for studying photoinduced charge
123 generation in mono- to few-layer semiconductors and a
124 promising strategy for synthetic engineering of mono- to few-
125 layer TMDCs for optoelectronic applications requiring high
126 yields of mobile excited-state charge carriers.
127

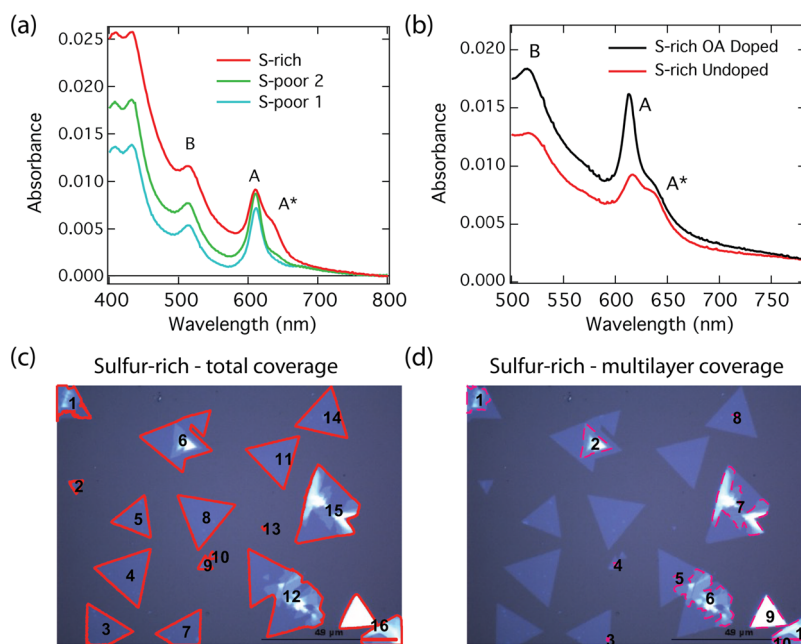


Figure 2. (a) Absorbance spectra of WS₂ samples grown with varying sulfur fluxes within the CVD growth process. (b) Absorbance spectra of a WS₂ sample grown in sulfur-rich conditions that is either undoped (red trace) or doped with the one-electron oxidant OA. (c) Optical microscopy image of sulfur-rich WS₂ sample. The solid red lines outline the area of the substrate covered by both monolayer and multilayer WS₂ triangles, as identified by an image segmentation algorithm via MATLAB. (d) The same optical microscopy image shown in panel c, where the dashed red lines outline the area of the sample covered by multilayer portions of WS₂. After imaging >50 flakes, the ratio of the multilayer area to the total area for this sample was estimated to be 28% (\pm 13%).

128 In this study, we synthesize mono- to few-layer WS₂ flakes on
 129 SiO₂/Si wafers by atmospheric pressure chemical vapor
 130 deposition (APCVD) and transfer them to quartz substrates.
 131 The absorption spectrum of a characteristic CVD-grown WS₂
 132 sample containing predominantly monolayer flakes (see analysis
 133 below) is shown in Figure 1a (solid blue line). The absorption
 134 spectrum of a sample dominated by WS₂ monolayers consists of
 135 three primary peaks corresponding to excitonic optical
 136 transitions: the A exciton at 611 nm (2.03 eV), the B exciton
 137 at 513 nm (2.42 eV), and the C exciton at 432 nm (2.87 eV).
 138 The primary excitonic photoluminescence (PL) occurs at 617
 139 nm (Figure 1a, dashed line), corresponding to a Stokes shift of
 140 20 meV, characteristic of monolayer WS₂. The samples consist
 141 of isolated and randomly oriented triangular flakes with edge
 142 lengths of ca. 20–100 μ m, as shown by a representative zoomed
 143 optical microscopy image of a monolayer flake in Figure 1b. In
 144 larger area optical images (Figure 1c), many flakes can be
 145 observed with a second layer or even multiple additional layers,
 146 as indicated by the sharp change in contrast. In Figure 1c, the
 147 flakes containing additional layers are indicated by asterisks.
 148 The spectroscopic signatures of mono- to few-layer WS₂
 149 depend strongly on the number of layers (Figures 1d–f and
 150 S1), providing additional means to confirm the presence of
 151 multilayer segments observed via optical microscopy. The PL
 152 intensity decreases rapidly with layer number (Figure 1d,f), as
 153 observed by others,^{7,48} and also shifts bathochromically from ca.
 154 620 nm to >640 nm (Figure 1d) in transitioning from
 155 monolayer to multilayer. Raman spectra (Figure 1e) of both
 156 mono- and multilayers show the expected in-plane E_{2g} mode at
 157 353 cm⁻¹ and the A_{1g} out-of-plane mode at 417 cm⁻¹, in addition
 158 to a number of acoustic combination modes.⁴⁸ The intensity
 159 ratio of the A_{1g} mode, relative to the E_{2g} mode, systematically
 160 increases with increasing layer number (Figure 1e,f), as
 161 previously observed for WS₂.^{48–50} The combination of

observations in Figure 1 demonstrate that both optical
 microscopy and confocal spectroscopy can be readily used to
 discern the presence and prevalence of both monolayers and
 multilayers in our CVD-grown WS₂.

It is generally appreciated that the CVD growth environment
 can play a significant role in the quality and optoelectronic
 properties of TMDCs, but it is often difficult to understand the
 mechanisms at play. We find that varying the sulfur flux in the
 CVD synthesis leads to dramatic changes in the WS₂ absorption
 spectrum. Figure 2a shows the absorbance spectra of three
 samples grown in either sulfur-rich or sulfur-deficient condi-
 tions. While all three samples display the optical transitions of
 the A, B, and C excitons, two of the samples show an appreciable
 shoulder (labeled A*) ca. 60 meV below the A exciton of
 monolayers, with an absorption maximum of approximately 630
 nm (1.97 eV). The presence of this shoulder also correlates with
 an appreciable rising background across all visible wavelengths.
 These observations are consistent with the changes in
 absorbance observed between monolayer and few-layer WS₂
 in several recent studies.^{51–54} Specifically, Niu et al. observed
 that the 2.02 eV A exciton energy of monolayer WS₂ shifts
 abruptly by ca. 40 meV to 1.98 eV in bilayer WS₂ and then more
 gradually shifts as the layer number increases (i.e., a total shift of
 ca. 60 meV for 3 layers and 80 meV for 6 layers).⁵¹ The
 transition from mono- to few-layer WS₂ is also accompanied by a
 significant broad absorption background,^{51,52} as observed for
 the samples in Figure 2a. We thus assign the A* peak to the
 excitonic transition of multilayer WS₂ portions of the samples.

To confirm that the A* peak observed in Figure 2a
 corresponds to the absorption of multilayer WS₂ areas, we
 must rule out other possible contributions and also attempt to
 correlate the absorption with structural information. Zhu et al.
 tentatively assigned a broad peak below the monolayer A exciton
 peak to the absorbance of an electron or hole-bound exciton

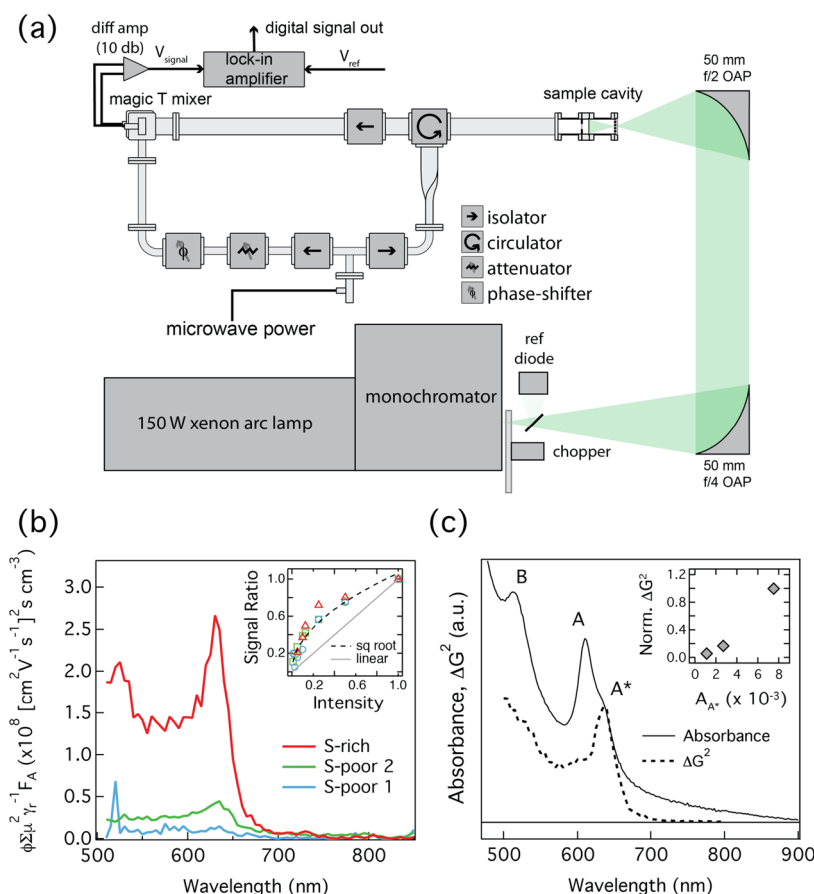


Figure 3. (a) Diagram of the microwave homodyne circuit used to conduct steady-state microwave conductivity (SSMC) experiments. (b) Photoconductance action spectra of the same three samples. Inset: fluence dependence of photoconductance, measured at 530 nm. Dashed line shows a square root dependence of photoconductance on light intensity, which fits the measured data significantly better than a linear regression (gray solid line). The percentage of multilayers extracted from microscopy images are $8.8 \pm 3.6\%$ for S-poor 1, $8.7 \pm 4.8\%$ for S-poor 2, and $28.3 \pm 13.2\%$ for S-rich. (c) Comparison of the absorbance spectrum (solid line) and photoconductance action spectrum (dashed line) of the sample synthesized under sulfur-rich conditions, after OA doping. Inset: normalized photoconductance as a function of the absorbance of the A^* exciton peak assigned to multilayers.

196 (negative or positive trion, respectively).²¹ Molas et al. observed
 197 two peaks in the reflectance spectrum of WS_2 monolayers at $T =$
 198 5 K, lower in energy by ca. 37 and 56 meV relative to the A
 199 exciton.⁵⁵ The strong sensitivity of each peak to the electro-
 200 statically gated charge carrier density in the WS_2 monolayer
 201 allowed for the assignment of both peaks to trion optical
 202 transitions (labeled T_1 and T_2 , respectively).⁵⁵ To probe
 203 whether the 630 nm peak in our spectra corresponds to a
 204 trion optical transition, we treated films with a well-known one-
 205 electron oxidant—triethyloxonium hexachloroantimonate
 206 (OA), which has been used as a p-type molecular dopant in a
 207 number of organic and low-dimensional materials.^{56–58} The
 208 absorption spectrum of an OA-doped film (Figure 2b)
 209 demonstrates that injection of holes by adsorbed OA molecules
 210 dramatically increases the oscillator strength of the A exciton.
 211 This observation suggests that the holes injected by OA
 212 molecules compensate a native electron density (that quenches
 213 the A exciton by phase space filling) to produce a WS_2 sample
 214 that is more electronically intrinsic. Importantly, the intensity of
 215 the A^* peak is unaffected by the same change in excess carrier
 216 density, suggesting that this absorbance feature is not related to
 217 the optical transition of trions. Analysis of PL spectra for the
 218 undoped and OA-doped S-rich sample also suggests that the free
 219 charge carriers measured in the microwave conductivity
 220 experiment do not result predominantly from direct optical

excitation of trions (Figure S2 and associated discussion in the
 Supporting Information).

For a window into the prevalence of multilayer areas in the
 WS_2 samples, we analyzed a large number of optical microscopy
 images of flakes. An algorithm was developed that used the
 difference in contrast (see Figure 2c) between mono- and
 multilayer sections to calculate the total area covered by each, as
 shown in Figure S3. Statistical analysis of a large number of flakes
 (>50) for the “S-poor 1” sample and the “S-rich” sample revealed
 that the relative area covered by multilayers in the latter sample
 was approximately four times more than that for the “S-deficient
 1” sample. This analysis corroborates the hypotheses that CVD
 growth in more sulfur-deficient conditions leads to the
 production of more multilayer WS_2 sections and that these
 multilayer sections contribute to a relatively strong excitonic
 transition (A^*) in the absorbance spectrum at ca. 630 nm.

To determine the degree to which optical excitation of either
 mono- or multilayer WS_2 optical transitions may give rise to free
 charge carriers, we turned to steady-state microwave con-
 ductivity. A schematic of our system is shown in Figure 3a. In
 this experiment we use lock-in detection to measure the change
 in photoconductance induced in the sample by square-wave
 optical excitation, recording the magnitude of the photo-
 conductance (ΔG) signal as a function of excitation wavelength
 to produce a photoconductance action spectrum. The chopping

246 frequency (73 Hz) is low enough that steady-state is reached
247 nearly instantaneously during each on-cycle. We use a new
248 microwave resonator and homodyne detection circuit designed
249 for this experiment; the latter is shown in Figure 3a. These
250 improvements confer 2 orders of magnitude greater sensitivity
251 than we typically obtain for fp-TRMC, making it possible to
252 measure weakly photoconductive samples with a monochro-
253 mated xenon lamp. The photoconductance is normalized to the
254 photon flux at each wavelength to produce photocurrent action
255 spectra, as shown in Figure 3b,c. Further details are provided in
256 the Experimental Section and the Supporting Information.

257 Figure 3b displays photoconductance action spectra for the
258 three samples plotted in Figure 2a. The y-axis is the steady-state
259 photoconductance figure of merit, which incorporates the yield,
260 mobility, and recombination rate constant of the charges we
261 detect. It is directly proportional to charge carrier yield per
262 incident photon at each excitation wavelength (see the
263 Supporting Information for details). Each sample produces
264 some amount of free charge carriers that can be measured by the
265 attenuation of the ca. 9 GHz microwave probe beam, and the
266 yield of photoinduced charge carriers depends on the excitation
267 wavelength. In particular, the samples all show a maximum in the
268 photoconductance for an excitation wavelength of 630 nm. The
269 photoconductance scales with the square root of the incident
270 light intensity (inset, Figure 3b), as expected for a second-order
271 bimolecular recombination process (see also Figure S4) such as
272 the diffusion-limited recombination of free charge carriers.

273 Figure 3c compares the photoconductance action spectrum
274 (dashed line) to the absorbance spectrum (solid line) of the OA-
275 doped sample synthesized under sulfur-rich conditions. This
276 comparison illustrates a remarkable correspondence between
277 the A* transition in the absorbance spectrum and the
278 predominant peak observed in the photoconductance action
279 spectrum. In contrast, the photoconductance spectrum does not
280 have a peak where the A exciton would be expected at ca. 611
281 nm, even though the oscillator strength of that monolayer
282 exciton transition has been largely restored by the OA doping
283 process. Interestingly, the photoconductance action spectrum
284 also has a pronounced peak at 525 nm, which is consistent with
285 the position of the B exciton observed for multilayer samples in
286 many recent studies.^{51–54} Thus, panels b and c of Figure 3
287 suggest that photoexcitation of WS₂ multilayers is the dominant
288 source of free charge carriers in the WS₂ samples, while direct
289 excitation of excitons in monolayers produces significantly fewer
290 charge carriers. The inset of Figure 3c supports this conclusion,
291 showing that the measured photoconductance (after correction,
292 see inset of Figure 3b) correlates linearly with the absorbance of
293 the A* exciton transition.

294 To discuss the mechanism of charge generation upon
295 photoexcitation of the A exciton in multilayer WS₂ (labeled
296 here as A*), we must take into account both thermodynamic and
297 kinetic considerations. It is first important to note that the
298 binding energy of the A exciton decreases dramatically with
299 increasing layer number in TMDCs.^{59,60} Theoretical studies
300 suggest that the A exciton binding energy in bilayer TMDCs can
301 be roughly half that of the monolayer⁶⁰ and can be reduced by an
302 order of magnitude for bulk relative to the monolayer.⁵⁹
303 Experimentally, Chernikov et al. found a binding energy of ca.
304 320 meV for monolayer WS₂^{61,62} and a reduction of the binding
305 energy in bulk WS₂ to ca. 50 meV,⁶² which is quite close to $k_B T$ at
306 room temperature (25 meV). The sharp reduction in binding
307 energy with increasing layer thickness should lead to a

corresponding increase in thermally induced exciton dissocia-
tion.

Associated with the reduction in binding energy for increasing
layer number is a higher degree of exciton delocalization over
multiple layers and an increased exciton size.⁶³ First-principles
calculations on mono- and few-layer TMDCs by Palummo et al.
suggest that this increased exciton delocalization leads to a
progressive slowing of radiative recombination with increasing
layer number.⁶³ This slower radiative recombination rate allows
for other nonradiative recombination processes to compete with
radiative recombination and quench PL in multilayer TMDCs.
Such nonradiative recombination pathways include thermal
dissociation of excitons, recombination across the indirect gap
following exciton dissociation, and carrier trapping. While the
slower radiative recombination of excitons can qualitatively
explain the numerous reports of reduced PL quantum yields in
multilayer TMDCs^{7,59,62} (see also Figure 1d,f), PL measure-
ments cannot provide information on the fate of nonemissive
excitons. The current study conclusively demonstrates that
some proportion of photogenerated excitons in multilayer WS₂
are spontaneously dissociated to produce free mobile charge
carriers.

To examine the possible role of defect states in producing
charges, we used the ab initio GW method to compute the band
structure (Figure S5a) and ab initio GW-BSE method to
compute the optical absorption (Figure S5b) of pristine
monolayer WS₂ and monolayer WS₂ containing sulfur vacancy
defects. We chose sulfur vacancy defects based on the common
observation of these defects in as-grown TMDCs⁶⁴ and the
suggested³⁹ (but debated)⁶⁵ link between such vacancies and
the n-type nature of as-grown TMDCs. The band structure
(Figure S5a) demonstrates that sulfur vacancies produce
partially filled donor states (c_D) near the conduction band and
acceptor states (v_D) lying within the valence band. Such defect
states could potentially contribute to free carrier generation in
the SSMC experiment. For example, an exciton could potentially
undergo dissociation into a localized bound electron sitting in
the defect donor state c_D and a hole in an extended defect state
 v_D that is hybridized with the valence band manifold.

Several peaks below the A exciton in the calculated defect-
containing WS₂ layer (Figure S5b) correspond to the presence
of optically active defect transitions. While the defects calculated
here may play a role in charge generation observed by SSMC,
several factors suggest that the optically active defect transitions
may not play a dominant role in direct charge generation by
excitation at the A* peak. First, the intensity of the A* peak in
the experimental absorbance spectrum is correlated with CVD
growth in sulfur-rich conditions, where one would assume the
number density of sulfur vacancies would likely diminish relative
to sulfur-poor growth conditions. Second, in an attempt to
discern the role of sulfur vacancies in the A* absorbance feature,
we annealed samples with prominent A* peaks in sulfur vapor in
our CVD chamber to see if we could “passivate” sulfur vacancies.
We did not observe any change in the A* absorbance intensity,
making it difficult to link this A* peak directly to sulfur vacancies.
The role of these trap states in exciton dissociation and charge
generation is thus an intriguing possibility, but the bulk of our
data suggests that the strong A* peak observed in the absorbance
and photoconductance spectra is primarily correlated with the
relative density of multilayers in the WS₂ samples.

As a final consideration for the source of the observed
spontaneous exciton dissociation in multilayer WS₂, we note
that our samples contain myriad junctions between monolayers

371 and multilayers. A number of recent studies have utilized
 372 scanning probe techniques to analyze the interfacial thermody-
 373 namics of such junctions, e.g. in MoS₂, MoSe₂, and WSe₂.^{66,67}
 374 These studies found the presence of both large band bending
 375 within the multilayer and interfacial trap states at the
 376 monolayer/multilayer interface. Examination of the resulting
 377 band diagrams suggests that photoexcitation in multilayers
 378 could lead to holes being trapped at the interface and electrons
 379 being repelled from the interface. While such studies have not
 380 been reported for WS₂, this type of interfacial band bending
 381 could potentially contribute to spontaneous exciton dissocia-
 382 tion, leaving one dominant type of mobile charge carrier that
 383 would contribute to our observed 9 GHz photoconductance.

384 The steady-state microwave conductivity technique devel-
 385 oped here is an important complement to time-resolved
 386 measurements on mono- to few-layer semiconductors and has
 387 additional advantages over such measurements. Transient
 388 absorption (TA) spectra of the sulfur-rich sample (Figure 4a)
 389 are dominated by a ground-state bleach (GSB) at 626 nm (A*),
 390 both at early and long pump-probe time delays, consistent with
 391 excitations (excitons, charges, or both) ending up primarily in
 392 the multilayer portions of the sample. In contrast, spectra for the
 393 S-poor 1 sample are dominated by the GSB of the A exciton at
 394 ca. 612 nm. The lifetime of the A* GSB in the S-rich sample is
 395 significantly longer than that of the A exciton GSB in the S-poor
 396 sample. While the TA spectra alone do not allow for assignment
 397 of the spectral features to charges and/or excitons, the much
 398 larger 9 GHz attenuation observed in SSMC experiments for the
 399 S-rich sample suggests that the long-lived GSB in the S-rich
 400 sample results from charges that are generated in the multilayer
 401 portions of the sample.

402 Time-resolved microwave conductivity transients (Figure 4c)
 403 demonstrate that the charges produced in the S-rich sample are
 404 long-lived, with an appreciable fraction of carriers surviving
 405 beyond 500 ns. The recombination lifetimes, extracted from
 406 global fits of the fluence-dependent transients (black lines,
 407 Figure 4c), decrease with increasing photon fluence (see also
 408 inset and Figure S6), consistent with the second-order
 409 bimolecular recombination mechanism inferred from SSMC
 410 (inset, Figure 3c). However, we cannot reliably estimate a
 411 yield from this data because of the fundamental difference
 412 between AC and DC mobility⁶⁸ and the lack of established
 413 values of μ_{AC} for WS₂.

414 Interestingly, the carrier lifetimes extracted from TRMC
 415 transients (tens to hundreds of nanoseconds, Figure S6) are
 416 much longer than those extracted from TA measurements (tens
 417 to hundreds of picoseconds). As discussed in detail by Levine et
 418 al., this discrepancy arises primarily from the much larger
 419 instantaneous carrier generation rate associated with the ca. 200
 420 fs pulse width of TA measurement, relative to the 4 ns pulse
 421 width of the TRMC measurement.⁶⁹ In addition, the lowest
 422 fluence used for the TRMC measurements reported here is
 423 $\sim 10\times$ lower than in the TA (8×10^{12} vs 7×10^{13} cm⁻²,
 424 respectively). We do not believe these lifetime estimates are
 425 substantially impacted by the instrument response time, as our
 426 fitting procedures⁷⁰ are capable of extracting components $\sim 10\times$
 427 smaller than the instrument response time of 7 ns and the fastest
 428 component extracted here was 3 ns at the highest fluence.
 429 However, we note that any process that takes place on a time
 430 scale faster than about one period of the microwave probe field
 431 (100 ps) will not be observed.

432 In contrast to both of these transient experiments, SSMC has
 433 the advantage of a low carrier generation rate that is on par with

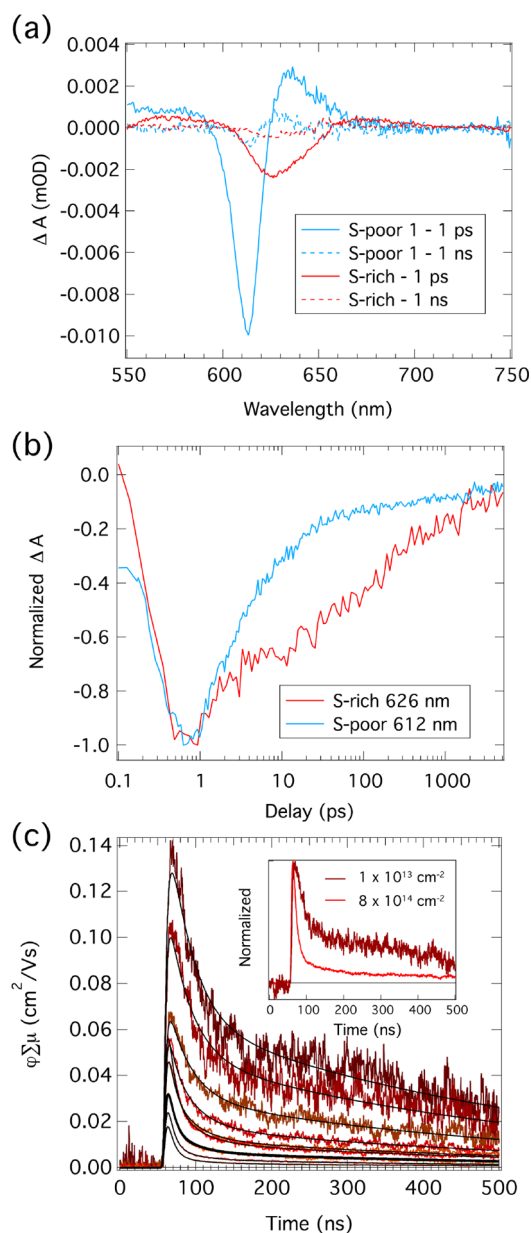


Figure 4. (a) Transient absorption spectra of S-rich and S-poor 1 samples at pump-probe delays of 1 ps and 1 ns. (b) Transient absorption dynamics of the S-rich and S-poor 1 samples, probed at 626 nm (A* exciton) and 612 nm (A exciton), respectively. (c) Fluence-dependent time-resolved microwave conductivity transients of the S-rich sample, following excitation at 640 nm (A* exciton). Fluence increases from ca. 8×10^{12} cm⁻² to ca. 8×10^{14} cm⁻², going from top to bottom transient. Inset: Normalized transients following low- and high-fluence excitation at 640 nm.

or lower than the generation rate associated with the solar flux. 434
 Moreover, for a rapid assessment of the photoconductance 435
 action spectra, the SSMC measurement offers several additional 436
 advantages over the TRMC measurement in terms of 437
 throughput, cost, and safety considerations. While TRMC can 438
 be used to produce photoconductance action spectra,^{27,33,44} 439
 such experiments can take a full day to run and analyze, as 440
 opposed to the 0.5–1 h time frame needed for a similar SSMC 441
 action spectrum. Additionally, the pulsed laser needed for 442
 TRMC measurements requires both a substantial financial 443
 investment and the establishment of both administrative and 444

445 engineering safety controls for class 4 laser operation, whereas
446 the CW light source of the SSMC technique is inexpensive and
447 operates at low photon fluences that pose no risk of eye damage.
448 In this study, we develop a specially fabricated steady-state
449 microwave conductivity experiment that is sensitive enough to
450 measure charge generation in a model mono- to few-layer WS₂
451 semiconductor upon excitation with light well below the solar
452 flux. We find that mobile charges are generated in WS₂ samples
453 primarily when photons directly excite the excitonic transition
454 (denoted here as A*) of WS₂ multilayers, while complementary
455 measurements suggest that in some scenarios trions and/or
456 defect states may contribute to charge generation as well. The
457 amount of multilayers are correlated with the flux of sulfur in the
458 CVD growth process, with sulfur-rich conditions producing
459 more WS₂ multilayers. Complementary TA and TRMC studies
460 confirm that the photogenerated charges reside primarily within
461 the multilayer portion of a sample grown in sulfur-rich
462 conditions and that such free charge carriers can survive well
463 beyond 500 ns when generated at fluences at or below solar
464 fluences. Controlling these long-lived free charges can be
465 important for enhancing surface catalytic reactions and
466 harvesting charges in photodetectors. The current study
467 demonstrates that the SSMC experiment has the sensitivity to
468 provide mechanistic information on charge carrier generation in
469 mono- to few-layer semiconductors, an extreme case where the
470 total absorption is less than 10 mOD and the charges are
471 generated in a thin slab of material ranging from ca. 0.7 to 4 nm
472 thick. These results suggest that the SSMC technique can be
473 used as a fast and inexpensive route toward measuring free
474 carrier generation in a wide variety of low-dimensional
475 semiconductors and heterojunctions, even for ultrathin samples
476 where the total density of generated charges is exceptionally low.

477 ■ EXPERIMENTAL SECTION

478 *Sample Preparation.* Monolayer WS₂ was grown on SiO₂/Si
479 wafers by atmospheric pressure chemical vapor deposition
480 (APCVD). For synthesizing monolayer WS₂, a water-soluble
481 precursor was coated on the SiO₂/Si substrate first. The
482 precursor solution was prepared by mixing three types of
483 chemical solutions (defined as A, B, and C).

- 484 • A (metal precursor): 0.2 g of ammonium metatungstate
485 (AMT, Sigma-Aldrich, 463922) was dissolved in 10 mL of
486 deionized (DI) water for tungsten precursor.
- 487 • B (promoter): 0.1 g of sodium hydroxide (NaOH, Sigma-
488 Aldrich, 795429) dissolved in 30 mL of DI water was
489 introduced for promoting monolayer TMDCs.
- 490 • C (medium solution): an OptiPrep density gradient
491 medium (Sigma-Aldrich, D1556, 60% (w/v) solution of
492 iodixanol in water) was used as a medium solution.

493 The precursor solution in which A, B, and C were mixed in
494 certain ratios was coated onto the SiO₂/Si wafer by spin-casting
495 at 3000 rpm for 1 min.

496 The precursor-coated substrate and 0.2 g of sulfur (Sigma,
497 344621) were separately introduced to a two-zone furnace. The
498 temperature of the sulfur zone was increased to 200 and 250 °C
499 for sulfur-poor and sulfur-rich conditions, respectively, to
500 modulate the portion of WS₂ multilayers. At the same time,
501 the substrate zone was increased to 800 °C at a rate of 100 °C/
502 min. Nitrogen (600 sccm) and hydrogen (10 sccm) gases were
503 injected as a carrier gas and reactive agent, respectively, to
504 reduce metal oxides.

The as-grown WS₂ on SiO₂/Si was transferred to a quartz 505
substrate for further optical measurement. Poly(methyl 506
methacrylate) (PMMA C4, MicroChem) was coated onto 507
samples as a supporting layer and then immersed into diluted 508
hydrofluoric acid for detaching WS₂ from the SiO₂/Si wafer by 509
etching silicon oxide. The PMMA-supported samples were 510
transferred to a quartz substrate, and then PMMA was removed 511
by acetone. 512

Characterization. Confocal Photoluminescence and Raman 513
Spectra. Confocal PL and Raman spectra of WS₂ monolayer 514
were acquired with an InVia Renishaw confocal Raman 515
microscope with a 532 nm laser. The laser power was measured 516
by a Thorlabs PM100D power meter. For the PL measurements, 517
the laser intensity was 260 W/cm². For the Raman measure- 518
ments, the laser intensity was 1.84 kW/cm². The PL/Raman 519
signals were dispersed by grating mirrors (600 lines/mm grating 520
for the PL measurements and 1800 lines/mm grating for the 521
Raman measurements) and detected by a charge-coupled device 522
(CCD) array. 523

Absorption Spectroscopy. The absorption of films was 524
measured using a Cary 5000 optical spectrophotometer in 525
transmission mode. The absorption is not corrected for 526
reflection. 527

Steady-State Microwave Conductivity. Steady-state implemen- 528
tations of microwave conductivity^{46,70} have rarely been 529
reported⁴³ but provide important complementary advantages 530
over pulsed-laser excitation. The simplicity of measuring a 531
steady-state microwave absorption signal allows parametric 532
study of new variables such as excitation wavelength or applied 533
magnetic field. In this Letter we present steady-state photo- 534
conductance action spectroscopy; this is similar to measuring a 535
photocurrent action spectrum, but with no electrical contacts. 536
We optimized our microwave circuit for sensitive detection of 537
square-wave modulated photoconductivity. This includes a high 538
quality factor microwave resonator^{46,56} ($Q = 850$), a low phase- 539
noise microwave source (Rhode & Schwartz SMB100A), a 540
homodyne detection circuit, and a lock-in amplifier (Stanford 541
Research, SR830). This apparatus is ~ 100 times more sensitive 542
than our standard fp-TRMC apparatus.⁴⁶ 543

Figure 3a shows a diagram of the microwave homodyne 544
circuit and optical path. The microwave probe is split into two 545
arms, reference and sample. The sample arm contains the sample 546
cavity, coupled to the circuit via a circulator; the reference arm 547
contains a variable phase shifter and attenuator. The two arms 548
rejoin at a hybrid (magic) tee, which has a pair of matched 549
Schottky barrier diode detectors (1N23C), one in each output 550
arm of the tee. Their differential sensitivity is measured using a 551
calibrated attenuator in order to quantify microwave power 552
absorption (Figure S7). The whole circuit is implemented in a 553
WR90 (X-band) waveguide, and the isolators and circulator (M- 554
Wave Design) all have a directivity of ≥ 35 dB. In operation, the 555
microwave frequency (~ 9.9 GHz, 100 mW) is tuned to 556
resonance with the sample cavity; the amplitude in each arm 557
is equalized, and the relative phase is set to 90°. Interference of 558
the reference and sample signals in the magic tee produces equal 559
output power at the two detectors; any change in sample 560
conductivity due to optical excitation manifests as an imbalance 561
of the two detector signals, which we acquire and selectively 562
amplify using a differential voltage amplifier (Teledyne LeCroy 563
DA1855) and a lock-in amplifier (Stanford Research SR830). 564

Excitation is provided by a 150 W xenon arc lamp coupled to a 565
monochromator (OBB Tunable Power Arc, 0.3 m f/4 566
monochromator, 1200 lp/mm grating). The output beam is 567

mechanically chopped (Stanford Research SR540) and sampled using an amplified photodiode to provide an excitation reference channel (acquired by a second lock-in, Stanford Research SR510). The remaining output is collimated by a 45° off-axis parabolic mirror (OAP, $f/4$, 50 mm dia., Edmonds Optics) and reimaged onto an opening in the sample cavity by a second OAP ($f/2$, 50 mm dia.). The latter optical relay configuration allows the microwave circuit to be placed as far as possible from the optical chopper while also maximizing optical coupling efficiency. The former consideration is important, as one of the main noise sources in the present instrument configuration is vibrational coupling with the optical chopper. Microwave-transparent polymer shims are used to prevent the sample from vibrating within the microwave cavity. We note that, as with our TRMC measurement, the SSMC measurement reported here measures the average photoconductance of the sample, because the visible excitation source and the microwave probe beam illuminate the entire 1×2 cm quartz substrate on which the sample is deposited.

Square wave optical excitation of the sample induces a square-wave modulation in its conductivity; microwave power is absorbed, and a square-wave amplitude modulation is encoded on the microwave probe. Interference with the reference arm demodulates this signal, which appears as a voltage difference between the two microwave detectors. The lock-in amplifier detects the first Fourier series component of this signal and returns its root-mean-squared amplitude. Thus, it follows that the peak-to-peak voltage modulation of the original square-wave signal is

$$\Delta V_S = \frac{\pi\sqrt{2}}{4} V_{LLA}$$

From this point the analysis is identical to that for fp-TRMC data. We calculate the change in microwave power reflection according to

$$\frac{\Delta P}{P} = n(V_{Cell}) \frac{\Delta V_S}{V_{Cell}}$$

where $n(V_{Cell})$ is an empirical calibration function that describes the sensitivity of the detector, and V_{Cell} is the equilibrium voltage output of the two detectors when the microwave frequency is on resonance with the cavity and the interferometer is balanced. The photoconductance is calculated as

$$\Delta G = -\frac{1}{K} \frac{\Delta P}{P}$$

where K is the sensitivity factor of the microwave cavity, calculated from electromagnetic simulations, which have been thoroughly described previously.⁴⁶ In the present case, $K = 198\,000$.

The final transformation we perform is to normalize the photoconductance by the photon flux at each excitation wavelength, which is calculated from the reference diode measurement and a calibration measurement using a NIST-traceable silicon photodiode (Newport 818-UV) mounted at the sample position. However, the relationship between steady-state photoconductance and light intensity depends on the recombination order that is obtained in any given sample. First-order recombination leads to a steady-state charge density that is linear with light intensity, whereas second-order recombination leads to a square-root dependence. In the present case, all the WS_2 samples displayed near-perfect square-root behavior,

suggesting that bimolecular recombination predominates. This is accounted for in calculating the figure of merit displayed in Figure 3b. See the Supporting Information for details.

Flash Photolysis Time-Resolved Microwave Conductivity. For TRMC measurements, the WS_2 samples were pumped with a 5 ns pulse width beam from an optical parametric oscillator (OPO) pumped by the third harmonic of an Nd:YAG laser and probed by microwaves at around 9 GHz. The microwave field is absorbed by photogenerated mobile carriers, and its relative change in power ΔP can be measured. The change in microwave power relates to the photoconductivity ΔG through $\Delta P/P = -K\Delta G$ where K is an empirically determined calibration factor for the microwave cavity used in this experiment. For the TRMC measurements reported here, $K = 24\,000$. The cavity response time is 7 ns. The photoconductivity is proportional to the number of charges and their mobility. It can be expressed as $\Delta G = e\beta F_A I_0 (\phi \Sigma \mu)$ where e is the elementary charge, $\beta = 2.2$ the geometric factor for the X-band waveguide used, I_0 the incident photon flux, F_A the fraction of light absorbed at the excitation wavelength, ϕ the quantum efficiency of free carrier generation per photon absorbed, and $\Sigma \mu = \mu_e + \mu_h$ the sum of the mobilities of electrons and holes. Biexponential fits of the photoconductivity decay transients were weighted to calculate the average carrier lifetime using the equation $\tau_{avg} = (A_0\tau_0 + A_1\tau_1)/(A_0 + A_1)$.

Transient Absorption Spectroscopy. Transient absorption spectra and dynamics were measured with an Ultrafast Systems laser system, using the “Helios” configuration, which employs pump and probe pulses with widths of ca. 200 fs and dynamic range for the pump–probe delay of ca. 5 ns. The system is based on a 1 kHz regeneratively amplified Ti:sapphire laser system that produces 4 mJ laser pulses at 800 nm. The Ti:sapphire laser pumps an optical parametric amplifier (OPA) to generate the 520 nm pump light. The excitation pulse energy employed for exciting the WS_2 samples was ca. 85 nJ at 520 nm, with a spot size of ca. 600 μm . A portion of the amplified 800 nm light was passed through a sapphire plate to generate the visible (400 nm $< \lambda_{probe} < 800$ nm) continuum probe pulse. The probe pulses were delayed in time with respect to the pump pulse using a motorized translation stage mounted with a retroreflecting mirror. All TA measurements were performed in an air-free optical holder to avoid sample degradation in the presence of oxygen and irradiation.

■ ASSOCIATED CONTENT

● Supporting Information

The Supporting Information is available free of charge at <https://pubs.acs.org/doi/10.1021/acs.jpcllett.9b03117>.

Additional results, analysis of photoluminescence, discussion of image analysis algorithm, and theoretical methods (PDF)

■ AUTHOR INFORMATION

Corresponding Authors

*E-mail: jeffrey.blackburn@nrel.gov.

*E-mail: obadiah.reid@colorado.edu, obadiah.reid@nrel.gov.

ORCID

Jeffrey L. Blackburn: 0000-0002-9237-5891

Hanyu Zhang: 0000-0001-9942-8186

Jeremy R. Dunklin: 0000-0003-0070-8167

Seok Joon Yun: 0000-0002-8695-7166

680 Young Hee Lee: 0000-0001-7403-8157
681 Elisa M. Miller: 0000-0002-7648-5433
682 Garry Rumbles: 0000-0003-0776-1462
683 Obadiah G. Reid: 0000-0003-0646-3981

684 Notes

685 The authors declare no competing financial interest.

686 ■ ACKNOWLEDGMENTS

687 S.J.Y. and Y.H.L. prepared the WS₂ monolayer samples and
688 acknowledge Institute for Basic Science (IBS-R011-D1) for
689 funding. O.G.R. and G.R. designed the SSMC experiment.
690 O.G.R., J.L.B., H.Z., A.R.M., R.N.H., D.C.C., and E.M.M.
691 performed spectroscopic studies, and D.V.-F. performed ab
692 initio calculations. These NREL coauthors are employees of the
693 Alliance for Sustainable Energy, LLC, the manager and operator
694 of the National Renewable Energy Laboratory for the U.S.
695 Department of Energy (DOE) under Contract No. DE-AC36-
696 08GO28308. Funding provided by the U.S. DOE, Office of
697 Science, Office of Basic Energy Sciences, Division of Chemical
698 Sciences, Geosciences, and Biosciences, Solar Photochemistry
699 Program.

700 ■ REFERENCES

701 (1) Butler, S. Z.; Hollen, S. M.; Cao, L.; Cui, Y.; Gupta, J. A.; Gutierrez,
702 H. R.; Heinz, T. F.; Hong, S. S.; Huang, J.; Ismach, A. F.; et al. Progress,
703 Challenges, and Opportunities in Two-Dimensional Materials Beyond
704 Graphene. *ACS Nano* **2013**, *7*, 2898–2926.
705 (2) Wilson, J. A.; Yoffe, A. D. The Transition Metal Dichalcogenides
706 Discussion and Interpretation of the Observed Optical, Electrical and
707 Structural Properties. *Adv. Phys.* **1969**, *18*, 193–335.
708 (3) Kumar, A.; Ahluwalia, P. K. Electronic Structure of Transition
709 Metal Dichalcogenides Monolayers 1h-Mx₂ (M = Mo, W; X = S, Se,
710 Te) from Ab-Initio Theory: New Direct Band Gap Semiconductors.
711 *Eur. Phys. J. B* **2012**, *85*, 186.
712 (4) Komsa, H.-P.; Kotakoski, J.; Kurasch, S.; Lehtinen, O.; Kaiser, U.;
713 Krasheninnikov, A. V. Two-Dimensional Transition Metal Dichalco-
714 genides under Electron Irradiation: Defect Production and Doping.
715 *Phys. Rev. Lett.* **2012**, *109*, 035503.
716 (5) Tedstone, A. A.; Lewis, D. J.; O'Brien, P. Synthesis, Properties, and
717 Applications of Transition Metal-Doped Layered Transition Metal
718 Dichalcogenides. *Chem. Mater.* **2016**, *28*, 1965–1974.
719 (6) Chen, Y.; Xi, J.; Dumcenco, D. O.; Liu, Z.; Suenaga, K.; Wang, D.;
720 Shuai, Z.; Huang, Y.-S.; Xie, L. Tunable Band Gap Photoluminescence
721 from Atomically Thin Transition-Metal Dichalcogenide Alloys. *ACS*
722 *Nano* **2013**, *7*, 4610–4616.
723 (7) Mak, K. F.; Lee, C.; Hone, J.; Shan, J.; Heinz, T. F. Atomically Thin
724 Mos₂: A New Direct-Gap Semiconductor. *Phys. Rev. Lett.* **2010**, *105*,
725 136805.
726 (8) Liu, Y.-H.; Porter, S. H.; Goldberger, J. E. Dimensional Reduction
727 of a Layered Metal Chalcogenide into a 1d near-Ir Direct Band Gap
728 Semiconductor. *J. Am. Chem. Soc.* **2012**, *134*, 5044–5047.
729 (9) Bettis Homan, S.; Sangwan, V. K.; Balla, I.; Bergeron, H.; Weiss, E.
730 A.; Hersam, M. C. Ultrafast Exciton Dissociation and Long-Lived
731 Charge Separation in a Photovoltaic Pentacene–Mos₂ Van Der Waals
732 Heterojunction. *Nano Lett.* **2017**, *17*, 164–169.
733 (10) Zhong, C.; Sangwan, V. K.; Wang, C.; Bergeron, H.; Hersam, M.
734 C.; Weiss, E. A. Mechanisms of Ultrafast Charge Separation in a Ptb₇/
735 Monolayer Mos₂ Van Der Waals Heterojunction. *J. Phys. Chem. Lett.*
736 **2018**, *9*, 2484–2491.
737 (11) Yuan, L.; Chung, T.-F.; Kuc, A.; Wan, Y.; Xu, Y.; Chen, Y. P.;
738 Heine, T.; Huang, L. Photocarrier Generation from Interlayer Charge-
739 Transfer Transitions in Ws₂-Graphene Heterostructures. *Science*
740 *Advances* **2018**, *4*, No. e1700324.
741 (12) Sulas-Kern, D. B.; Zhang, H.; Li, Z.; Blackburn, J. L. Microsecond
742 Charge Separation at Heterojunctions between Transition Metal

Dichalcogenide Monolayers and Single-Walled Carbon Nanotubes. *743*
Mater. Horiz. **2019**, *6*, 2103–2111. *744*
(13) Kang, D.-H.; Kim, M.-S.; Shim, J.; Jeon, J.; Park, H.-Y.; Jung, W.-
745 S.; Yu, H.-Y.; Pang, C.-H.; Lee, S.; Park, J.-H. High-Performance *746*
Transition Metal Dichalcogenide Photodetectors Enhanced by Self-
747 Assembled Monolayer Doping. *Adv. Funct. Mater.* **2015**, *25*, 4219–
748 4227. *749*
(14) Wang, H.; Zhang, C.; Chan, W.; Tiwari, S.; Rana, F. Ultrafast *750*
Response of Monolayer Molybdenum Disulfide Photodetectors. *Nat.*
751 *Commun.* **2015**, *6*, 8831. *752*
(15) Yin, Z.; Li, H.; Li, H.; Jiang, L.; Shi, Y.; Sun, Y.; Lu, G.; Zhang, Q.; *753*
Chen, X.; Zhang, H. Single-Layer Mos₂ Phototransistors. *ACS Nano* *754*
2012, *6*, 74–80. *755*
(16) Jiang, H. Electronic Band Structures of Molybdenum and *756*
Tungsten Dichalcogenides by the Gw Approach. *J. Phys. Chem. C* **2012**, *757*
116, 7664–7671. *758*
(17) Jaramillo, T. F.; Jorgensen, K. P.; Bonde, J.; Nielsen, J. H.; Horch, *759*
S.; Chorkendorff, I. Identification of Active Edge Sites for Electro-
760 chemical H₂ Evolution from Mos₂ Nanocatalysts. *Science* **2007**, *317*,
761 100–102. *762*
(18) Benson, E. E.; Zhang, H.; Schuman, S. A.; Nanayakkara, S. U.; *763*
Bronstein, N. D.; Ferrere, S.; Blackburn, J. L.; Miller, E. M. Balancing *764*
the Hydrogen Evolution Reaction, Surface Energetics, and Stability of *765*
Metallic Mos₂ Nanosheets Via Covalent Functionalization. *J. Am.*
766 *Chem. Soc.* **2018**, *140*, 441–450. *767*
(19) Sun, T.; Zhang, H.; Wang, X.; Liu, J.; Xiao, C.; Nanayakkara, S. *768*
U.; Blackburn, J. L.; Mirkin, M. V.; Miller, E. M. Nanoscale Mapping of *769*
Hydrogen Evolution on Metallic and Semiconducting MoS₂ Nano-
770 sheets. *Nanoscale Horizons* **2019**, *4*, 619. *771*
(20) Laursen, A. B.; Kegnæs, S.; Dahl, S.; Chorkendorff, I. *772*
Molybdenum Sulfides—Efficient and Viable Materials for Electro-
773 and Photoelectrocatalytic Hydrogen Evolution. *Energy Environ. Sci.* *774*
2012, *5*, 5577–5591. *775*
(21) Zhu, B.; Chen, X.; Cui, X. Exciton Binding Energy of Monolayer *776*
Ws₂. *Sci. Rep.* **2015**, *5*, 9218. *777*
(22) Berkelbach, T. C.; Hybertsen, M. S.; Reichman, D. R. Theory of *778*
Neutral and Charged Excitons in Monolayer Transition Metal *779*
Dichalcogenides. *Phys. Rev. B: Condens. Matter Mater. Phys.* **2013**, *88*,
780 045318. *781*
(23) Ugeda, M. M.; Bradley, A. J.; Shi, S.-F.; da Jornada, F. H.; Zhang, *782*
Y.; Qiu, D. Y.; Ruan, W.; Mo, S.-K.; Hussain, Z.; Shen, Z.-X.; et al. Giant *783*
Bandgap Renormalization and Excitonic Effects in a Monolayer *784*
Transition Metal Dichalcogenide Semiconductor. *Nat. Mater.* **2014**, *785*
13, 1091. *786*
(24) Mak, K. F.; He, K.; Lee, C.; Lee, G. H.; Hone, J.; Heinz, T. F.; *787*
Shan, J. Tightly Bound Trions in Monolayer Mos₂. *Nat. Mater.* **2013**, *788*
12, 207–211. *789*
(25) Kang, H. S.; Sisto, T. J.; Peurifoy, S.; Arias, D. H.; Zhang, B.; *790*
Nuckolls, C.; Blackburn, J. L. Long-Lived Charge Separation at *791*
Heterojunctions between Semiconducting Single-Walled Carbon *792*
Nanotubes and Perylene Diimide Electron Acceptors. *J. Phys. Chem.*
793 *C* **2018**, *122*, 14150–14161. *794*
(26) Dowgiallo, A.-M.; Mistry, K. S.; Johnson, J. C.; Blackburn, J. L. *795*
Ultrafast Spectroscopic Signature of Charge Transfer between Single-
796 Walled Carbon Nanotubes and C60. *ACS Nano* **2014**, *8*, 8573–8581. *797*
(27) Bindl, D. J.; Ferguson, A. J.; Wu, M.-Y.; Kopidakis, N.; Blackburn, *798*
J. L.; Arnold, M. S. Free Carrier Generation and Recombination in *799*
Polymer-Wrapped Semiconducting Carbon Nanotube Films and *800*
Heterojunctions. *J. Phys. Chem. Lett.* **2013**, *4*, 3550–3559. *801*
(28) Ceballos, F.; Bellus, M. Z.; Chiu, H.-Y.; Zhao, H. Ultrafast *802*
Charge Separation and Indirect Exciton Formation in a Mos₂–Mose₂ *803*
Van Der Waals Heterostructure. *ACS Nano* **2014**, *8*, 12717–12724. *804*
(29) Jin, C.; Ma, E. Y.; Karni, O.; Regan, E. C.; Wang, F.; Heinz, T. F. *805*
Ultrafast Dynamics in Van Der Waals Heterostructures. *Nat.* *806*
Nanotechnol. **2018**, *13*, 994–1003. *807*
(30) Hong, X.; Kim, J.; Shi, S.-F.; Zhang, Y.; Jin, C.; Sun, Y.; Tongay, *808*
S.; Wu, J.; Zhang, Y.; Wang, F. Ultrafast Charge Transfer in Atomically *809*
Thin Mos₂/Ws₂ Heterostructures. *Nat. Nanotechnol.* **2014**, *9*, 682. *810*

- 811 (31) Zhu, T.; Yuan, L.; Zhao, Y.; Zhou, M.; Wan, Y.; Mei, J.; Huang, L.
812 Highly Mobile Charge-Transfer Excitons in Two-Dimensional Ws₂/
813 Tetracene Heterostructures. *Science Advances* **2018**, *4*, No. eaao3104.
- 814 (32) Huang, Y. L.; Zheng, Y. J.; Song, Z.; Chi, D.; Wee, A. T. S.; Quek,
815 S. Y. The Organic-2d Transition Metal Dichalcogenide Heterointer-
816 face. *Chem. Soc. Rev.* **2018**, *47*, 3241–3264.
- 817 (33) Park, J.; Reid, O. G.; Blackburn, J. L.; Rumbles, G. Photoinduced
818 Spontaneous Free-Carrier Generation in Semiconducting Single-
819 Walled Carbon Nanotubes. *Nat. Commun.* **2015**, *6*, 8809.
- 820 (34) Cunningham, P. D.; McCreary, K. M.; Hanbicki, A. T.; Currie,
821 M.; Jonker, B. T.; Hayden, L. M. Charge Trapping and Exciton
822 Dynamics in Large-Area Cvd Grown Mos₂. *J. Phys. Chem. C* **2016**, *120*,
823 5819–5826.
- 824 (35) Docherty, C. J.; Parkinson, P.; Joyce, H. J.; Chiu, M.-H.; Chen,
825 C.-H.; Lee, M.-Y.; Li, L.-J.; Herz, L. M.; Johnston, M. B. Ultrafast
826 Transient Terahertz Conductivity of Monolayer Mos₂ and Wse₂
827 Grown by Chemical Vapor Deposition. *ACS Nano* **2014**, *8*, 11147–
828 11153.
- 829 (36) Hu, Z.; Wu, Z.; Han, C.; He, J.; Ni, Z.; Chen, W. Two-
830 Dimensional Transition Metal Dichalcogenides: Interface and Defect
831 Engineering. *Chem. Soc. Rev.* **2018**, *47*, 3100–3128.
- 832 (37) Zhang, S.; Dong, N.; McEvoy, N.; O'Brien, M.; Winters, S.;
833 Berner, N. C.; Yim, C.; Li, Y.; Zhang, X.; Chen, Z.; et al. Direct
834 Observation of Degenerate Two-Photon Absorption and Its Saturation
835 in Ws₂ and Mos₂ Monolayer and Few-Layer Films. *ACS Nano* **2015**, *9*,
836 7142–7150.
- 837 (38) Li, Y.; Dong, N.; Zhang, S.; Zhang, X.; Feng, Y.; Wang, K.; Zhang,
838 L.; Wang, J. Giant Two-Photon Absorption in Monolayer Mos₂. *Laser*
839 *& Photonics Reviews* **2015**, *9*, 427–434.
- 840 (39) Ugeda, M. M.; Bradley, A. J.; Shi, S.-F.; da Jornada, F. H.; Zhang,
841 Y.; Qiu, D. Y.; Ruan, W.; Mo, S.-K.; Hussain, Z.; Shen, Z.-X.; et al. Giant
842 Bandgap Renormalization and Excitonic Effects in a Monolayer
843 Transition Metal Dichalcogenide Semiconductor. *Nat. Mater.* **2014**,
844 *13*, 1091–1095.
- 845 (40) Steinhoff, A.; Florian, M.; Rosner, M.; Schonhoff, G.; Wehling, T.
846 O.; Jahnke, F. Exciton Fission in Monolayer Transition Metal
847 Dichalcogenide Semiconductors. *Nat. Commun.* **2017**, *8*, 1166.
- 848 (41) Cunningham, P. D.; Hanbicki, A. T.; McCreary, K. M.; Jonker, B.
849 T. Photoinduced Bandgap Renormalization and Exciton Binding
850 Energy Reduction in Ws₂. *ACS Nano* **2017**, *11*, 12601–12608.
- 851 (42) Yuan, L.; Wang, T.; Zhu, T.; Zhou, M.; Huang, L. Exciton
852 Dynamics, Transport, and Annihilation in Atomically Thin Two-
853 Dimensional Semiconductors. *J. Phys. Chem. Lett.* **2017**, *8*, 3371–3379.
- 854 (43) Labram, J. G.; Perry, E. E.; Venkatesan, N. R.; Chabiny, M. L.
855 Steady-State Microwave Conductivity Reveals Mobility-Lifetime
856 Product in Methylammonium Lead Iodide. *Appl. Phys. Lett.* **2018**,
857 *113*, 153902.
- 858 (44) Ferguson, A. J.; Dowgiallo, A.-M.; Bindl, D. J.; Mistry, K. S.; Reid,
859 O. G.; Kopidakis, N.; Arnold, M. S.; Blackburn, J. L. Trap-Limited
860 Carrier Recombination in Single-Walled Carbon Nanotube Hetero-
861 junctions with Fullerene Acceptor Layers. *Phys. Rev. B: Condens. Matter*
862 *Mater. Phys.* **2015**, *91*, 245311.
- 863 (45) Ihly, R.; Mistry, K. S.; Ferguson, A. J.; Clikeman, T. T.; Larson, B.
864 W.; Reid, O. G.; Boltalina, O. V.; Strauss, S. H.; Rumbles, G.; Blackburn,
865 J. L. Tuning the Driving Force for Exciton Dissociation in Single-Walled
866 Carbon Nanotube Heterojunctions. *Nat. Chem.* **2016**, *8*, 603–609.
- 867 (46) Reid, O. G.; Moore, D. T.; Li, Z.; Zhao, D.; Yan, Y.; Zhu, K.;
868 Rumbles, G. Quantitative Analysis of Time-Resolved Microwave
869 Conductivity Data. *J. Phys. D: Appl. Phys.* **2017**, *50*, 493002.
- 870 (47) Reid, O. G.; Yang, M.; Kopidakis, N.; Zhu, K.; Rumbles, G.
871 Grain-Size-Limited Mobility in Methylammonium Lead Iodide Perov-
872 skite Thin Films. *ACS Energy Letters* **2016**, *1*, 561–565.
- 873 (48) Berkdemir, A.; Gutierrez, H. R.; Botello-Mendez, A. R.; Perea-
874 Lopez, N.; Elías, A. L.; Chia, C.-I.; Wang, B.; Crespi, V. H.; Lopez-Urías,
875 F.; Charlier, J.-C.; et al. Identification of Individual and Few Layers of
876 Ws₂ Using Raman Spectroscopy. *Sci. Rep.* **2013**, *3*, 1755.
- 877 (49) Gutierrez, H. R.; Perea-Lopez, N.; Elías, A. L.; Berkdemir, A.;
878 Wang, B.; Lv, R.; Lopez-Urías, F.; Crespi, V. H.; Terrones, H.;
Terrones, M. Extraordinary Room-Temperature Photoluminescence in
879 Triangular Ws₂ Monolayers. *Nano Lett.* **2013**, *13*, 3447–3454.
- 880 (50) Kim, H.-C.; Kim, H.; Lee, J.-U.; Lee, H.-B.; Choi, D.-H.; Lee, J.-
881 H.; Lee, W. H.; Jhang, S. H.; Park, B. H.; Cheong, H.; et al. Engineering
882 Optical and Electronic Properties of Ws₂ by Varying the Number of
883 Layers. *ACS Nano* **2015**, *9*, 6854–6860.
- 884 (51) Niu, Y.; Gonzalez-Abad, S.; Frisenda, R.; Maruhn, P.; Druppel,
885 M.; Gant, P.; Schmidt, R.; Taghavi, N. S.; Barcons, D.; Molina-
886 Mendoza, A. J.; et al. Thickness-Dependent Differential Reflectance
887 Spectra of Monolayer and Few-Layer Mos₂, Mose₂, Ws₂ and Wse₂.
888 *Nanomaterials* **2018**, *8*, 725.
- 889 (52) Zhao, W.; Ghorannevis, Z.; Chu, L.; Toh, M.; Kloc, C.; Tan, P.-
890 H.; Eda, G. Evolution of Electronic Structure in Atomically Thin Sheets
891 of Ws₂ and Wse₂. *ACS Nano* **2013**, *7*, 791–797.
- 892 (53) Chowdhury, R. K.; Nandy, S.; Bhattacharya, S.; Karmakar, M.;
893 Bhaktha, S. N. B.; Datta, P. K.; Taraphder, A.; Ray, S. K. Ultrafast Time-
894 Resolved Investigations of Excitons and Biexcitons at Room Temper-
895 ature in Layered Ws₂. *2D Mater.* **2019**, *6*, 015011.
- 896 (54) Vega-Mayoral, V.; Vella, D.; Borzda, T.; Prijatelj, M.; Tempra, I.;
897 Pogna, E. A. A.; Dal Conte, S.; Topolovsek, P.; Vujicic, N.; Cerullo, G.;
898 et al. Exciton and Charge Carrier Dynamics in Few-Layer Ws₂.
899 *Nanoscale* **2016**, *8*, 5428–5434.
- 900 (55) Molas, M. R.; Nogajewski, K.; Slobodeniuk, A. O.; Binder, J.;
901 Bartos, M.; Potemski, M. The Optical Response of Monolayer, Few-
902 Layer and Bulk Tungsten Disulfide. *Nanoscale* **2017**, *9*, 13128–13141.
- 903 (56) Ferguson, A. J.; Reid, O. G.; Nanayakkara, S. U.; Ihly, R.;
904 Blackburn, J. L. Efficiency of Charge-Transfer Doping in Organic
905 Semiconductors Probed with Quantitative Microwave and Direct-
906 Current Conductance. *J. Phys. Chem. Lett.* **2018**, *9*, 6864–6870.
- 907 (57) MacLeod, B. A.; Stanton, N. J.; Gould, I. E.; Wesenberg, D.; Ihly,
908 R.; Owczarczyk, Z. R.; Hurst, K. E.; Fewox, C. S.; Folmar, C. N.;
909 Holman Hughes, K.; et al. Large N- and P-Type Thermoelectric Power
910 Factors from Doped Semiconducting Single-Walled Carbon Nanotube
911 Thin Films. *Energy Environ. Sci.* **2017**, *10*, 2168–2179.
- 912 (58) Avery, A. D.; Zhou, B. H.; Lee, J.; Lee, E.-S.; Miller, E. M.; Ihly,
913 R.; Wesenberg, D.; Mistry, K. S.; Guillot, S. L.; Zink, B. L.; et al.
914 Tailored Semiconducting Carbon Nanotube Networks with Enhanced
915 Thermoelectric Properties. *Nature Energy* **2016**, *1*, 16033.
- 916 (59) Komsa, H.-P.; Krashenninnikov, A. V. Effects of Confinement and
917 Environment on the Electronic Structure and Exciton Binding Energy
918 of Mos₂ from First Principles. *Phys. Rev. B: Condens. Matter Mater. Phys.*
919 **2012**, *86*, 241201.
- 920 (60) Cheiwchanchamnangij, T.; Lambrecht, W. R. L. Quasiparticle
921 Band Structure Calculation of Monolayer, Bilayer, and Bulk Mos₂.
922 *Phys. Rev. B: Condens. Matter Mater. Phys.* **2012**, *85*, 205302.
- 923 (61) Hill, H. M.; Rigosi, A. F.; Roquelet, C.; Chernikov, A.;
924 Berkelbach, T. C.; Reichman, D. R.; Hybertsen, M. S.; Brus, L. E.;
925 Heinz, T. F. Observation of Excitonic Rydberg States in Monolayer
926 Mos₂ and Ws₂ by Photoluminescence Excitation Spectroscopy. *Nano*
927 *Lett.* **2015**, *15*, 2992–2997.
- 928 (62) Chernikov, A.; Berkelbach, T. C.; Hill, H. M.; Rigosi, A.; Li, Y.;
929 Aslan, O. B.; Reichman, D. R.; Hybertsen, M. S.; Heinz, T. F. Exciton
930 Binding Energy and Nonhydrogenic Rydberg Series in Monolayer Ws₂.
931 *Phys. Rev. Lett.* **2014**, *113*, 076802.
- 932 (63) Palumbo, M.; Bernardi, M.; Grossman, J. C. Exciton Radiative
933 Lifetimes in Two-Dimensional Transition Metal Dichalcogenides. *ACS*
934 *Nano Lett.* **2015**, *15*, 2794–2800.
- 935 (64) Carozo, V.; Wang, Y.; Fujisawa, K.; Carvalho, B. R.; McCreary,
936 A.; Feng, S.; Lin, Z.; Zhou, C.; Perea-Lopez, N.; Elías, A. L.; et al.
937 Optical Identification of Sulfur Vacancies: Bound Excitons at the Edges
938 of Monolayer Tungsten Disulfide. *Science Advances* **2017**, *3*,
939 No. e1602813.
- 940 (65) Singh, A.; Singh, A. K. Origin of π -Type Conductivity of
941 Monolayer Mos_2 . *Phys. Rev. B: Condens. Matter Mater. Phys.* **2019**, *99*,
942 121201.
- 943 (66) Zhang, C.; Chen, Y.; Huang, J.-K.; Wu, X.; Li, L.-J.; Yao, W.;
944 Tersoff, J.; Shih, C.-K. Visualizing Band Offsets and Edge States in
945 Bilayer–Monolayer Transition Metal Dichalcogenides Lateral Hetero-
946 junction. *Nat. Commun.* **2016**, *7*, 10349.

- 948 (67) Howell, S. L.; Jariwala, D.; Wu, C.-C.; Chen, K.-S.; Sangwan, V.
949 K.; Kang, J.; Marks, T. J.; Hersam, M. C.; Lauhon, L. J. Investigation of
950 Band-Offsets at Monolayer–Multilayer Mos₂ Junctions by Scanning
951 Photocurrent Microscopy. *Nano Lett.* **2015**, *15*, 2278–2284.
- 952 (68) Prins, P.; Grozema, F. C.; Schins, J. M.; Siebbeles, L. D. A.
953 Frequency Dependent Mobility of Charge Carriers Along Polymer
954 Chains with Finite Length. *Phys. Status Solidi B* **2006**, *243*, 382–386.
- 955 (69) Levine, I.; Gupta, S.; Bera, A.; Ceratti, D.; Hodes, G.; Cahen, D.;
956 Guo, D.; Savenije, T. J.; Avila, J.; Bolink, H. J.; et al. Can We Use Time-
957 Resolved Measurements to Get Steady-State Transport Data for Halide
958 Perovskites? *J. Appl. Phys.* **2018**, *124*, 103103.
- 959 (70) Savenije, T. J.; Ferguson, A. J.; Kopidakis, N.; Rumbles, G.
960 Revealing the Dynamics of Charge Carriers in Polymer:Fullerene
961 Blends Using Photoinduced Time-Resolved Microwave Conductivity.
962 *J. Phys. Chem. C* **2013**, *117*, 24085–24103.